

All-Dielectric Meta-Optics for High-Efficiency Independent Amplitude and Phase Manipulation

Brian O. Raeker, Hanyu Zheng, You Zhou, Ivan I. Kravchenko, Jason Valentine,* and Anthony Grbic*

Optical metasurfaces, composed of subwavelength scattering elements, demonstrate remarkable control over the transmitted amplitude, phase, and polarization of light. However, manipulating the amplitude upon transmission, without the use of surface waves, requires loss if a single metasurface is used. Herein, high-efficiency independent manipulation of the amplitude and phase of a beam is described using two lossless phase-only metasurfaces separated by a distance. With this configuration, optical components such as combined beam-forming and splitting devices are experimentally demonstrated, as well as those for forming complex-valued, 3D holograms. The compound meta-optic platform provides a promising approach for achieving high-performance holographic displays and compact optical components, while exhibiting a high overall efficiency.

1. Introduction

Controlling the amplitude, phase, and polarization of an optical field is essential to many applications in a broad range of scientific and industrial areas. Conventionally, this is achieved using a sequence of optical components such as lenses, polarizers, gratings, and amplitude masks. Such an approach results in physically large systems and reduced efficiency, especially if transmission loss is used to control the amplitude profile of the optical wave. As demand increases for compact and high-efficiency optical systems, optical metasurfaces offer a path toward satisfying such requirements. Metasurfaces are 2D arrays of subwavelength scatterers,

designed to exhibit remarkable control over the transmitted phase, amplitude, and polarization of light. Specifically, the ability to locally control the transmission characteristics provides a powerful approach to realizing flat optical components and systems with improved performance.^[1–4] This has been shown through a variety of devices, including flat lenses,^[5,6] beam-splitters,^[7–12] holograms,^[13–17] multiplexers,^[18–20] augmented reality displays,^[21] high-definition displays,^[22] image differentiation,^[23] and compact optical spectrometers.^[24] However, optical applications requiring spatial manipulation of the amplitude profile have relied on reflection,^[25] absorption,^[26] local polarization-dependent interference effects,^[19] or polarization conversion loss,^[11,12,14–18] resulting in lower efficiencies.

Independently controlling the spatial amplitude and phase distributions of an electromagnetic wave is essential to forming optical components such as combined beam-former and splitter devices. Metasurface optical beam-splitters have been demonstrated through a variety of methods^[7–12]; however, the beam shape is not altered, and efficiency is reduced due to diffraction or the use of loss. The use of evanescent surface waves to reshape the transmitted amplitude profile without loss or reflection has been theoretically shown at microwave frequencies^[27–30] and demonstrated in acoustics.^[31] However, evanescent fields can lead to bandwidth reductions, fabrication difficulties due to the required extreme subwavelength feature sizes, and exacerbated losses. Another use of amplitude and phase control is in forming 3D holograms, which can be produced with high quality if a specific complex-valued field profile is formed.^[16] Polarization loss has been used to form 3D holograms^[14–17] by performing a spatially varying polarization conversion across


B. O. Raeker, A. Grbic
Department of Electrical Engineering and Computer Science
University of Michigan
Ann Arbor, MI 48109, USA
E-mail: agrbic@umich.edu

H. Zheng
Department of Electrical Engineering and Computer Science
Vanderbilt University
Nashville, TN 37212, USA

Y. Zhou
Photonics Initiative
Adv. Science Research Center
City University of New York
New York, NY 10031, USA

I. I. Kravchenko
Center for Nanophase Materials Sciences
Oak Ridge National Laboratory
Oak Ridge, TN 37831, USA

J. Valentine
Department of Mechanical Engineering
Vanderbilt University
Nashville, TN 37212, USA
E-mail: jason.g.valentine@vanderbilt.edu

 The ORCID identification number(s) for the author(s) of this article can be found under <https://doi.org/10.1002/adpr.202100285>.

© 2021 The Authors. Advanced Photonics Research published by Wiley-VCH GmbH. This is an open access article under the terms of the Creative Commons Attribution License, which permits use, distribution and reproduction in any medium, provided the original work is properly cited.

DOI: 10.1002/adpr.202100285

the metasurface. Amplitude control is implemented by filtering the unconverted polarization component, while phase control is implemented via another metasurface parameter. While capable of producing high-quality holographic images, the efficiency of such devices is low and application-specific due to reliance on polarization loss.

Compound meta-optics are sequential metasurfaces separated by a distance and arranged along a common axis, which perform functions beyond the capabilities of individual metasurfaces. The configuration of the compound meta-optic is shown in **Figure 1a**. A process for designing paired phase-only metasurfaces was previously developed to implement independent amplitude and phase control.^[32,33] This process was verified through full-wave simulation at near-infrared wavelengths to form high-efficiency combined beam-former and splitters and a high-quality, 3D hologram.^[33] In this work, we experimentally demonstrate high-efficiency, independent amplitude and phase control over an optical field using compound meta-optics, moving beyond previous simulation-based verification to show the feasibility of the concept under realistic fabrication limitations.

Using the design approach, the spatial separation of the metasurfaces enables high-efficiency amplitude control by redistributing the optical beam amplitude instead of using loss to form the desired amplitude distribution. Alternative methods have also been developed to optimize sequential metasurfaces for spatial complex-valued control over a wave. Optimizing metasurface unit cell parameters using the adjoint optimization method,^[34] optimizing the plane wave spectrum,^[35] and optimizing equivalent current distributions^[36] have been used to design sequential metasurface systems. Additionally, a variety of applications have been demonstrated with sequential metasurface devices: aberration correction,^[37] optical retro-reflection,^[38] full-color holography,^[39] optical secret sharing,^[40] and optical diffractive neural networks.^[41,42] However, independent amplitude and phase control for arbitrary field profiles has not been explicitly demonstrated.

The compound meta-optic is formed by two lossless phase-only metasurfaces separated by a physically short distance of

homogeneous dielectric, as shown in **Figure 1a**. Together, they provide the desired independent amplitude and phase control. Adding additional metasurfaces would allow more control over the optical field (e.g., multi-wavelength performance^[6,25,34] or diffractive neural networks^[34,41,42] for multi-input multi-output applications), but only two metasurfaces are necessary for amplitude and phase control at a single wavelength. An alternative theoretical approach would be to utilize surface waves to reshape the amplitude and phase^[27–31]; however, this poses significant fabrication difficulties at optical wavelengths. As a result, we use two metasurfaces implementing local transformations on an incoming wave. As a proof of concept, we report experimental demonstrations of meta-optics that combine beam-forming and splitting, and produce high-quality, 3D holograms. The efficiency of the devices is high, only limited by the minor reflection from each metasurface. Here, we show the promise of optical compound meta-optics for high-efficiency holographic displays and optical components.

2. Results

2.1. Concept and Design of Compound Meta-Optics

The proposed compound meta-optic devices consist of two phase-only metasurfaces, each impressing a phase discontinuity onto an incident wave. The design method has been developed and verified in simulation at microwave frequencies^[32] and near-infrared wavelengths.^[33] The first metasurface applies a transmission phase discontinuity onto the known incident wave. This phase shift is designed so that the desired electric field amplitude distribution is formed at a distance equal to the separation distance between the metasurfaces. However, the phase of this field profile is incorrect relative to the desired output phase profile. Therefore, the second metasurface applies a phase correction to form the desired complex-valued electric field distribution. Essentially, the transmission phase shift provided by the first metasurface plus propagation across the separation distance provides amplitude control, and the second metasurface

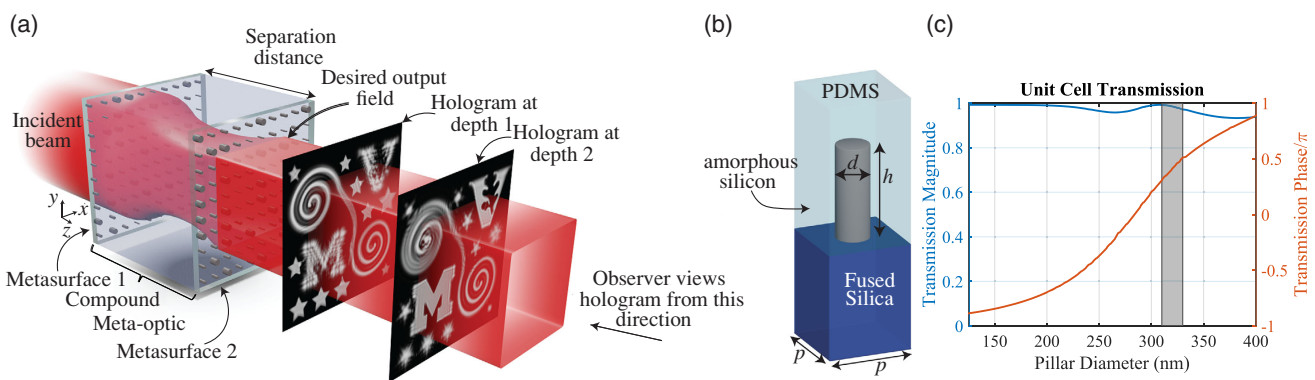


Figure 1. Diagram of the optical compound meta-optic and unit cell elements. a) Illustration of a compound meta-optic converting a uniform illumination into a 3D, complex-valued hologram. The meta-optic consists of sequential metasurfaces separated by a dielectric region. b) A schematic of the metasurface unit cell. Each cell has a period $p = 570$ nm and contains an amorphous silicon nanopillar with a height $h = 850$ nm. The diameter is varied across the metasurface to implement the desired transmission phase profile. c) Transmission characteristics of the unit cell under plane wave illumination and periodic boundary conditions. Diameters of 310–330 nm are not used in the 3D hologram designs due to observed low transmission in fabrication, which impacts the image quality.

provides phase control but does not adjust the amplitude. As these components can be designed independently, independent amplitude and phase control is achieved.

As the metasurfaces are each assumed to be transparent (ideally 100% transmission across each metasurface), the amplitude distributions of the wave transmitted by metasurface 1 and incident on metasurface 2 are known from the incident and desired field profiles, respectively. The free parameters are the transmission phase distributions at each plane, which are optimized using a phase-retrieval algorithm that links the incident and output field amplitude distributions. Specifically, the Gerchberg–Saxton phase-retrieval algorithm^[43] is modified to operate over short distances instead of the near-to-far-field conversion typically used. The phase shift distribution of each metasurface is calculated as the difference between the phase distributions of the transmitted and incident fields

$$\phi_{ms1} = \phi_{tr1} - \phi_{E_{inc}} \quad (1)$$

$$\phi_{ms2} = \phi_{E_{out}} - \phi_{inc2} \quad (2)$$

where $\phi_{E_{inc}}$ is the phase of the incident field, ϕ_{tr1} is the optimized phase profile of the transmitted field from metasurface 1, ϕ_{inc2} is the optimized phase of the field incident on metasurface 2, and $\phi_{E_{out}}$ is the phase profile of the desired output field. The metasurfaces are then designed to implement ϕ_{ms1} and ϕ_{ms2} as a transmission phase shift of the form $e^{i\phi_{ms}}$ on the incident wave. Here, a time convention of $e^{-i\omega t}$ is assumed.

Each metasurface is a dense array of silicon nanopillars, which are commonly used to implement desired spatial phase and polarization modulations with high transmission efficiency.^[1–4] Figure 1b shows a schematic of the unit cell, with the silicon nanopillar embedded in a layer of polydimethylsiloxane (PDMS) at the interface of a fused silica handle wafer. Circular cross sections of the nanopillars were chosen to ensure polarization invariance and reduce fabrication error risk; however, elliptical^[44] or rectangular^[12,16,25,45] cross sections could be used if polarization control is required. A more intricate nanopillar cross-sectional shape could also be used to further optimize the performance for other applications. Variation of the pillar

diameter (d) provides control over the transmission phase. The silicon pillar height ($h = 850$ nm), unit cell period ($p = 570$ nm), and illuminating wavelength ($\lambda_0 = 1.3$ μm) have been chosen to provide high transmittance for a large transmission phase range. The locally periodic approximation^[46,47] is made to determine the unit cell transmission by assuming that the nanopillars are placed in a homogeneous array environment. This approximation is commonly used to simplify the design of unit cells in inhomogeneous arrays and is generally accurate if the unit cells are not strongly coupled (as is the case here). Figure 1c shows the transmission for the chosen dimensions as a function of pillar diameter. For these dimensions, a transmission phase coverage of 78% can be achieved with a transmission magnitude greater than 0.93, which is essential for high-efficiency devices. Note that the pillar diameters of 125–400 nm are used in the beam-splitter designs, but 310–330 nm are not used in the 3D hologram design. This is due to the observed low transmission for these diameters in measurement, which impacts image quality. (Additional details about the unit cell design can be found in Supplementary Note 1.)

The phase shift profiles producing the desired amplitude and phase conversion of the input field are sampled at the unit cell periodicity and converted to distributions of nanopillars with the corresponding diameters. Each metasurface is then fabricated individually and aligned to form the compound meta-optic devices.

2.2. Fabrication and Characterization of Compound Meta-Optics

The meta-optic devices were fabricated using nanofabrication techniques developed to construct multi-metasurface devices.^[6,25] First, an 850 nm-thick layer of amorphous silicon was deposited onto a fused silica substrate. Each metasurface pattern was defined using electron beam lithography (EBL), and then nanopillars were formed using reactive ion etching (RIE).^[6,23,25] The metasurfaces were subsequently enclosed in a protective layer of PDMS. **Figure 2a** shows optical images of

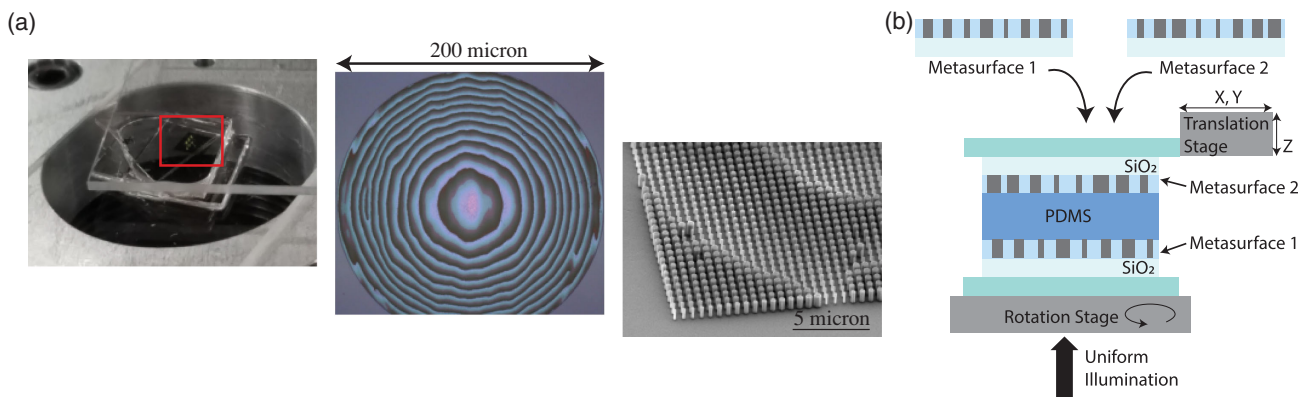


Figure 2. Fabricated meta-optic and schematic of meta-optic assembly. a) Left: An optical image of the fabricated meta-optic device, where the two metasurface layers are being aligned. Middle: Optical image of a fabricated metasurface, showing the variation in pillar diameter as a change in color. Right: A scanning electron microscope image of a portion of one metasurface, showing the array of silicon nanopillars. b) Schematic of the meta-optic assembly, alignment, and characterization process. Each metasurface is fabricated individually and then aligned to form the meta-optic device.

the meta-optic devices and one fabricated metasurface, and a scanning electron microscope image of the circular silicon nanopillars after RIE. Finally, the metasurfaces were spaced by a layer of PDMS and carefully aligned using translation stages to form the complete compound meta-optic, as shown in Figure 2b. Accurate alignment between the two metasurfaces ($< 1.5 \mu\text{m}$ lateral x, y -direction misalignment and $< 15 \mu\text{m}$ in the z -direction) is necessary to obtain the desired complex-valued field transformation.

To achieve the desired 3D alignment, we developed hologram alignment marks formed by silicon arrays fabricated near each of the two metasurfaces. (Additional information can be found in Supplementary Note 2.) First, a smaller array of silicon nanopillars near metasurface 1 was designed to form a phase-only hologram at a distance equal to the separation distance between the two metasurfaces. Similarly, an array of reflective silicon nanopillars was fabricated on the same layer as metasurface 2, designed to form the outline of the phase-only hologram projected from the first layer. The position of layer 2 was adjusted until the reflective outline exactly encompassed the phase-only hologram formed by layer 1.

The approach used here enables successful alignment for each two-metasurface device, avoiding a need to fabricate additional copies to improve alignment. After spatial alignment was achieved with the alignment marks, the alignment was further adjusted until the desired intensity image was formed at a distance beyond the meta-optic output. Misalignment introduces phase error to the output field distribution, and the output field phase defines the propagation behavior of the wave, so the alignment improves as the observed intensity image improves.

The compound meta-optics were characterized using an unpolarized supercontinuum laser whose beam is passed through a monochromator to select the desired wavelength. The resulting beam overfilled the meta-optic footprint to form the desired uniform illumination. The meta-optic performs the required spatial amplitude and phase manipulation to form the desired complex-valued output field distribution. Intensity distributions at different depths from the meta-optic output were then magnified with an objective and tube lens, and then recorded with a camera. Amplitude control over the incident optical field can be directly verified by imaging the output plane of the meta-optic. If the output field phase distribution is accurate, propagation of the output field will form the desired intensity profile at each plane in space beyond the meta-optic. However, if the phase distribution is inaccurate, the desired intensity will not be formed at a distance beyond the meta-optic. Therefore, phase control was verified by comparing the measured intensity distribution at a plane beyond the meta-optic output.

To demonstrate the accuracy of the compound meta-optic in providing independent phase and amplitude control with high efficiency, two different functions are presented. First, we show a combined beam-forming and splitting function where a uniform illumination is reshaped to form multiple output beams with specified amplitude profiles and propagation directions. Second, we design meta-optics to reshape a uniform illumination to form computer-generated, 3D holograms.

2.3. Meta-Optics for Combined Beam-Forming and Splitting

Using this design process, we designed, fabricated, and measured two meta-optic devices performing optical beam-forming and splitting at a wavelength of $\lambda_0 = 1.3 \mu\text{m}$. In both examples, circular uniform illumination with a diameter of $200 \mu\text{m}$ is reshaped to form multiple output Gaussian beams. Each metasurface is $200 \mu\text{m}$ in diameter and separated by $325 \mu\text{m}$ of PDMS. The first meta-optic forms the interference pattern between two Gaussian beams of different beamwidths, propagation directions, and relative intensities. The desired output field profile is calculated as the superposition of the two Gaussian beams as

$$E_{\text{out}} = -e^{-(\tau/45.5\lambda_0)^2} e^{ik_0 x \sin(-2^\circ)} + \sqrt{0.5} e^{-(\tau/32.5\lambda_0)^2} e^{ik_0 x \sin(2^\circ)} \quad (3)$$

which forms a fringed interference pattern. As the exact complex-valued field distribution is formed, only the desired Gaussian beams are produced and will separate as the optical field propagates away from the meta-optic output. Therefore, no undesired beams or diffraction orders are present, and the input field distribution is beam-formed and steered to produce only the desired beams at the output. Each metasurface of the device was simulated using the open-source finite-difference time-domain (FDTD) solver MEEP,^[48] and their responses combined to determine the overall meta-optic output field distribution. (Additional information about the meta-optic designs can be found in Supplementary Note 3.)

The amplitude profile of the incident field is redistributed as the wave propagates across the separation distance between the metasurfaces and can be visualized by observing the simulated field amplitude profile at various distances after the first metasurface. **Figure 3** shows the evolution of the simulated optical field amplitude as the wave propagates away from metasurface 1. The field transmitted by metasurface 1 has a uniform amplitude and closely matches the input field amplitude. However, due to the transmission phase imparted by metasurface 1, the optical field amplitude profile changes as the wave propagates. Eventually, the desired amplitude pattern is formed by the wave incident on metasurface 2. This combination implements amplitude control by the meta-optic. By placing metasurface 2 in the correct location relative to this field profile, a phase correction is applied (phase control), and the desired complex-valued output field is formed.

Figure 4a compares the intensity profiles formed by the meta-optic at the output plane (just after the second metasurface) and at a far-field distance for simulation and measurement. In each case, we see that the measurements closely agree with the simulated intensity distributions and form the desired Gaussian beams with little diffractive noise. Furthermore, the transformation in amplitude and phase was performed with an efficiency of 81% in simulation and 72% in measurement. The efficiency is defined as the fraction of intensity in the uniform illumination contained within the beam cross sections (with Fresnel reflection correction).

The second beam-former and splitter example was fabricated to produce three output Gaussian beams. The propagation directions are chosen such that the output field has variations in both planar dimensions (see Supplementary Note 3 for design specifics). **Figure 4b** compares the intensity profiles formed by

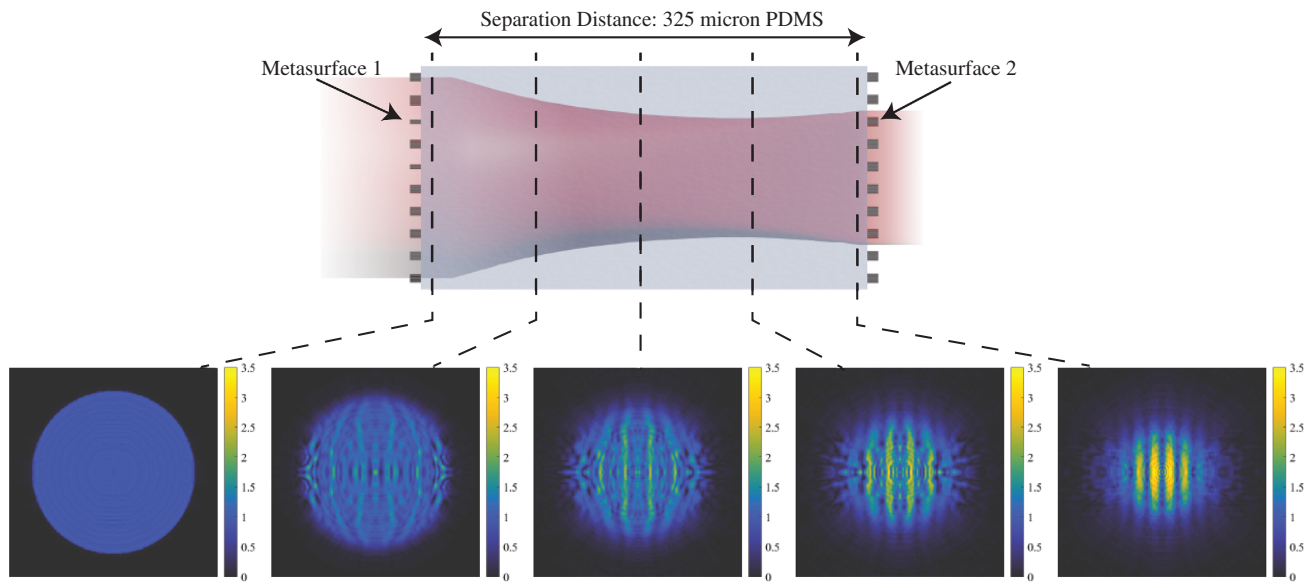


Figure 3. Evolution of the simulated optical field amplitude within the meta-optic. The optical field amplitude begins as a uniform distribution, but changes to form the desired Gaussian beam interference pattern amplitude as the wave propagates. The second metasurface provides a phase correction to form the desired complex-valued output field.

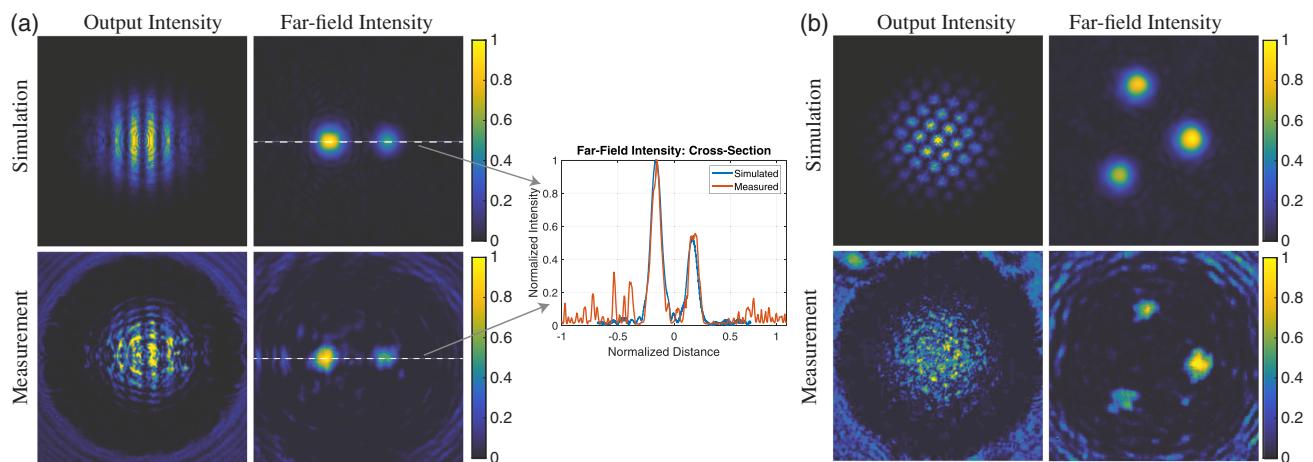


Figure 4. Measurement results of meta-optics implementing a beam-forming and splitting function. Meta-optics were designed to transform a uniform circular illumination into multiple Gaussian beams at the output. In each case, measurements closely match the simulation results. Note that intensities have been normalized to respective maximums. a) Two Gaussian beams are formed by the meta-optic. The output intensity is the characteristic fringing pattern of two interfering beams, verifying that the amplitude distribution of the optical field has been reshaped. The two beams appear separate at a far-field distance, verifying that the phase distribution at the output is also correct. A cross section through the beams is taken to show that the Gaussian profile of each beam is accurately formed. b) Three Gaussian beams are formed by a meta-optic. The output intensity is the interference pattern between the three beams and verifies that the amplitude profile has been reshaped. Three separate beams are observed at a far-field distance, matching simulation results. (Perceptually uniform color bar^[56] used for these and all following plots.)

the meta-optic at the output plane and a far-field distance in simulation to measurements. Here, the desired Gaussian beams are formed at the correct relative intensities, propagation directions, and beamwidths, verifying the accuracy of amplitude and phase control performed by the meta-optic. The device efficiency is 79% in simulation and 65% in measurement. One reason for the slight reduction in experimental efficiency of the beam-splitter devices is an experimentally observed transmission dip for pillars with diameters in the 310–330 nm range. This feature is

discussed in more detail in Supplementary Note 1. While we have demonstrated forming Gaussian beams here, any desired beam profile can be created as the meta-optic can explicitly form the desired amplitude and phase profiles.

2.4. Meta-Optics for 3D Holograms

Another exciting application of high-efficiency amplitude and phase control is 3D holography. While phase-only metasurfaces

can produce holograms, the resulting images inherently include speckle, which reduces the image quality. Phase and amplitude control allows for enhanced image quality, especially for 3D holograms, and significantly reduces the presence of speckle in images.^[13,16] Such complex-valued holograms have been generated using lossy methods, most commonly polarization loss^[14–17] or reflection.^[25] Here, we utilize the meta-optic design approach to demonstrate high-efficiency, 3D holograms. Multiple computer-generated hologram approaches can be used to display a 3D scene,^[49] but we demonstrate two methods: a simple point-source hologram and a hologram composed of solid flat image components^[50–52] more applicable to generating a realistic hologram scene.

Point-source holograms approximate the surface of a 3D object with a collection of point sources and have the advantage of wide viewing angles due to the diverging spherical wave from each point source. The field distribution at the meta-optic output that forms the hologram is calculated by summing the complex conjugated radiated fields from each point source. Phase-only

metasurfaces can implement such holograms by directly applying the phase of this field distribution to the incident field to form images. However, image quality is notably improved if the amplitude pattern is also formed.

Here, a compound meta-optic is designed to form the complex-valued interference field of point sources tracing the outline of the University of Michigan and Vanderbilt University logos. Each logo is tilted about its center by 15° to provide depth to the image, as shown in **Figure 5a**. The metasurfaces, designed to operate at $\lambda_0 = 1.1 \mu\text{m}$, were square arrays 200 μm in extent and separated by a distance of 275 μm (see Supplementary Note 3 for additional design details and different unit cell dimensions). **Figure 5b** compares the simulated hologram to the measured hologram at different depths, where the in-focus portion of each image is marked with a red arrow. We see that the measured intensity images closely match the desired intensity images with very little speckle noise.

While point-source holograms have wide viewing angles, they are unable to visually re-create the appearance of a realistic scene

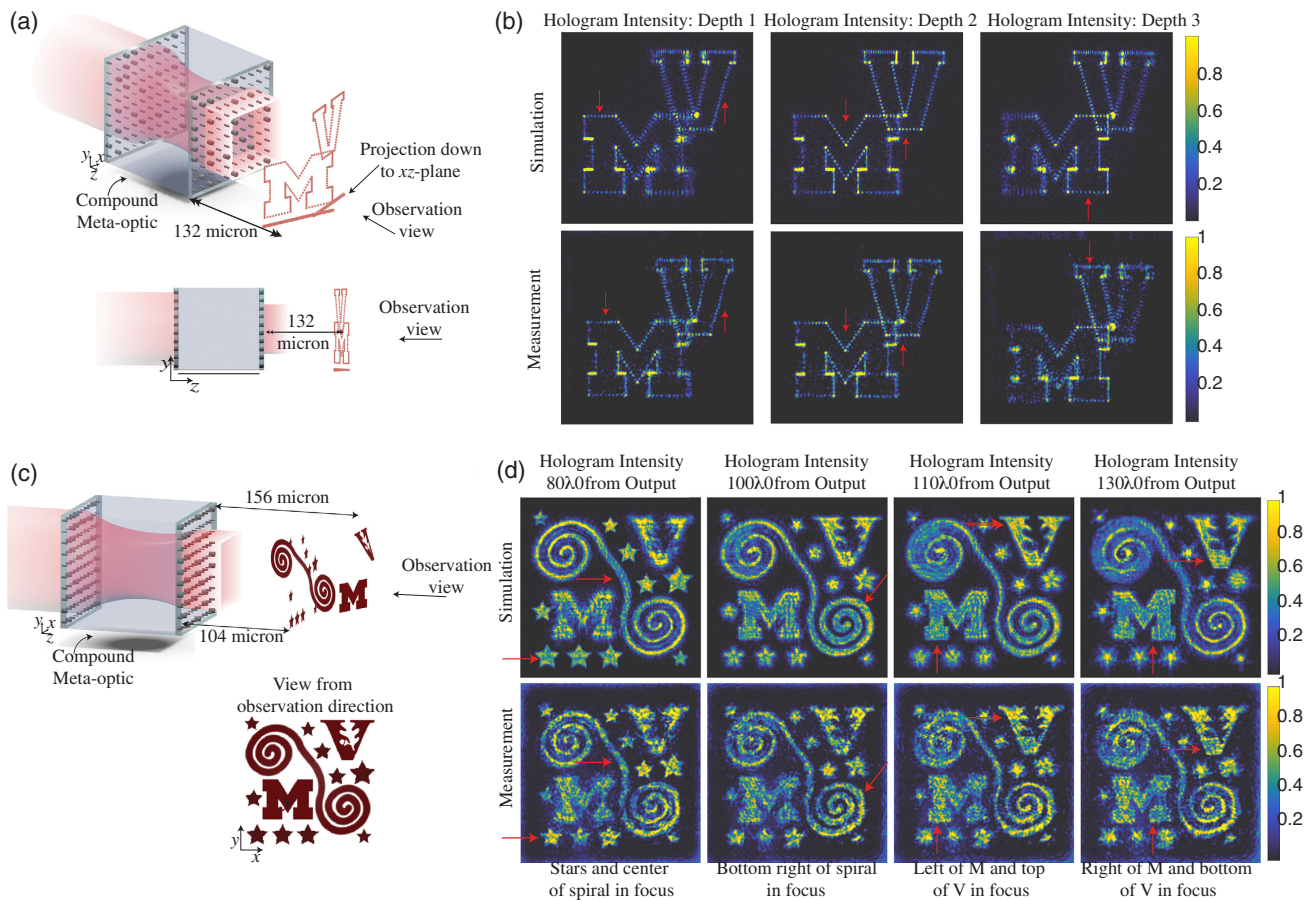


Figure 5. Comparison of simulation and measurement results of compound meta-optics implementing 3D holograms. In each case, the measurement results closely match the expected simulation results. Note that intensities are normalized to respective maximums. a) A point source hologram formed by a compound meta-optic at $\lambda_0 = 1.1 \mu\text{m}$. The University of Michigan and Vanderbilt University logos are tilted in space by 15°, providing depth to the hologram. b) The hologram intensity was recorded at different distances from the output plane of the compound meta-optic, showing that different portions of the hologram are in focus at different depths (as denoted by the red arrows). c) A 3D hologram using solid image components is formed by a compound meta-optic at $\lambda_0 = 1.3 \mu\text{m}$. The large spiral, University of Michigan, and Vanderbilt University logos are tilted in space to provide depth to the scene, while the stars are formed in the same plane, at the halfway point of the spiral. d) The hologram intensity was recorded at different distances from the meta-optic output, showing the different image components coming into and out of focus.

due to the point-based sampling of the surface. Next, we use computer-generated hologram techniques to generate a 3D hologram consisting of solid image components tilted in space.^[50–52] These techniques can be used to produce a faceted representation of an object, leading to the ability of forming 3D holograms of life-like scenes.^[33,50–52]

For this example, we designed a compound meta-optic where each metasurface is a 200 μm square array of nanopillars and separated by 325 μm of PDMS. The operating wavelength is $\lambda_0 = 1.3 \mu\text{m}$. The output field of the compound meta-optic was engineered in amplitude and phase to form the scene shown in Figure 5c. The large spiral, University of Michigan (M), and Vanderbilt University (V) logos are all tilted in space, but in different directions (see Supplementary Note 3 for additional design details). As a result, different cross sections of the image come into focus when imaging different depths from the meta-optic output plane. Figure 5d shows intensity images measured at different depths in the 3D hologram, which closely match the simulated images. Specifically, the first image shows the middle of the spiral and stars in focus, while the remaining images show different cross sections of the logos. The full 3D nature of the hologram can be seen by scanning the focal plane through the volume of the hologram, as shown in Video 1, Supporting Information, where the different image components clearly come in and out of focus. The compound meta-optic performs the desired complex-valued field manipulation with a simulated efficiency of 82% and measured efficiency of 75% for this example, significantly exceeding the efficiency of loss-based approaches.^[14–16,25] The efficiency considered here is the percentage of the input intensity present in the transmitted field distribution at the output of the meta-optic.

3. Discussion

The measured intensity images from each of the meta-optic devices demonstrate the accuracy of complex-valued optical field control with high efficiency. Specifically, the intensity measured at the output plane of the meta-optic demonstrates amplitude control as the uniform illumination is reshaped. The intensity measured at a plane beyond the aperture (after the optical field propagates away from the meta-optic output) demonstrates phase control as the desired intensity will only be formed if the output phase profile is accurate. An inaccurate phase profile would alter the propagation characteristics of the optical field so that the measured intensity pattern would not match the desired result. This is verified in Figure 4, where combined beam-former and splitters are demonstrated to form intensity distributions that closely match the expected distributions. Even though a small number of Gaussian beams were formed with these devices, meta-optics can be designed to produce a larger number of beams or beams with non-Gaussian amplitude profiles. The measured efficiency of the beam-former and splitter designs of 78% and 65% is higher than that of methods that would require loss. These values are only slightly lower than simulated efficiencies of 81% and 79%, respectively.

Similarly, the measured 3D holograms shown in Figure 5 very closely match the desired intensity images, demonstrating that the meta-optics can produce life-like holograms. The images

produced in Figure 5d with phase and amplitude control avoid the image speckle common to phase-only implementations produced with phase-retrieval algorithms.^[16] Furthermore, scanning the imaging plane through the hologram shows that the image components are accurately reproduced at the desired spatial locations (see Video 1, Supporting Information). This approach also maintains the image contrast compared to the desired phase profile simply applied to the uniform illumination (see Supplementary Note 4 for comparison). While the fabricated meta-optics demonstrated relatively simple holograms, meta-optics can be designed to form 3D holograms of life-like scenes.

High-efficiency amplitude and phase control over optical fields enable compound meta-optics to explicitly perform a variety of applications without inherent losses in efficiency. In contrast, loss-based amplitude control significantly reduces the device efficiency. For example, a measured efficiency of 6.4% was demonstrated in forming a complex-valued hologram using polarization conversion at THz frequencies.^[17] (However, intrinsic unit cell losses also contributed, as the measured efficiency for a similar phase-only version was 19.1%). Even when unit cells are optimized to obtain a maximum polarization conversion efficiency of 100%, the overall efficiency of a device is less than unity and highly case-dependent due to variation of transmission amplitude over the metasurface.^[16] Therefore, there are two main advantages of the compound meta-optic approach in terms of efficiency. First, using polarization loss for amplitude control requires a specific input polarization, which decreases the overall efficiency if an unpolarized source is used. Instead, the method shown here is polarization-independent and avoids this issue. Second, the efficiency of loss-based approaches is highly case-dependent, but compound meta-optics demonstrated here can achieve near-unity efficiency (in the ideal case) regardless of the required amplitude control. As a result, the measured 75% efficiency of the compound meta-optic producing the solid-image 3D hologram is significantly higher than lossy methods^[14–17] and is approximately independent of the desired amplitude control. This value is only slightly lower than the simulated efficiency of 82%.

The reduced measured efficiency relative to simulation is attributed to fabrication errors, in particular, an experimental transmission dip for pillars with diameters in the 310–330 nm range (in the case of the beam-splitting devices), and misalignment of the two metasurfaces. Fabrication errors and misalignment can also lead to phase errors in the output field distribution, causing slight degradation in image quality observed between simulation and experiment. Additionally, as a locally periodic approximation was used to design the metasurfaces, differences between the local periodic performance of each unit cell and inhomogeneous metasurface performance contribute to reduced efficiency and image quality. Optimizing the inhomogeneous metasurface structure^[53,54] could lead to improvements in efficiency and transmission phase accuracy. That said, the demonstrated compound meta-optics already exhibit amplitude and phase control with high efficiency and accuracy.

4. Conclusion

In conclusion, we have demonstrated compound meta-optics consisting of paired, lossless metasurfaces that independently

manipulate the amplitude and phase distributions of an optical field with high efficiency. Each metasurface was implemented as a high-transmission array of amorphous silicon nanopillars and aligned, operating at near-infrared wavelengths. The distance between the metasurfaces allows the optical wave to be reshaped, leading to high-efficiency devices by avoiding loss-based amplitude-control mechanisms. High-efficiency field control expands the application space of meta-optics, while maintaining a compact form factor.

As examples, we have experimentally shown that compound meta-optics can implement optical functions such as combined beam-forming and splitting, as well as form 3D holograms with high image quality. In each case, the measured efficiency of the fabricated meta-optic devices ranged between 65% and 75%, surpassing methods which rely on loss. By explicitly forming the desired complex-valued field profiles, no energy is lost to diffraction and high-quality holograms are obtained.

The compound meta-optic approach can be extended to visible optical wavelengths by a change in materials. For example, titanium dioxide can be used in place of silicon to fabricate the nanopillars.^[5,55] Additionally, polarization control can be achieved through an anisotropic nanopillar cross section. Furthermore, the transparent, phase-only control requirement of each metasurface could be implemented with liquid crystal designs for dynamic devices. Compound meta-optics could lead to improved performance in 3D holography, compact holographic displays, custom optical elements, and other applications requiring detailed control over the phase, amplitude, and polarization distributions of an optical field.

5. Experimental Section

Numerical Simulation Method: An open-source FDTD solver MEEP^[48] was used to simulate the transmission performance of the silicon nanopillar unit cells and each metasurface composing the meta-optics. The unit cells were individually simulated with periodic boundary conditions, while the metasurface simulation used perfectly matched layer boundaries 2 μm from the metasurface edge. The source field distribution was placed 1.5 μm in front of the metasurface or unit cell, and a field monitor was placed 1.5 μm after to record the transmission field amplitude and phase. To simulate the performance of the entire compound meta-optic, the transmitted field from the simulation of metasurface 1 was numerically propagated across the separation distance using the plane wave spectrum and used as the source for the FDTD simulation of metasurface 2. The transmitted field from the FDTD simulation of metasurface 2 was considered the output field of the meta-optic and compared to the measurement results.

The efficiency of each device was calculated from the simulation results by dividing the power contained in the output field distribution by the power of the field distribution illuminating the meta-optic. The efficiencies of the beam-former and splitter devices were calculated from the output power contained in each beam in the spectral domain/far-field. The efficiency of the 3D hologram device was calculated from the transmitted power of the device.

Fabrication Method: The metasurface patterns were defined on an 850 nm thick amorphous Si wafer, which was grown on a fused silica substrate using low-pressure chemical vapor deposition. A 200 nm thick polymethyl methacrylate (PMMA) A4 was spin-coated at 4500 rpm, followed by the deposition of 10 nm thick chromium as the conduction layer using thermal evaporation. The metasurface structures were defined using EBL, followed by the deposition of 35 nm thick aluminum oxide as the

dry etch mask using e-beam evaporation. The Si nanoposts were then formed by RIE using a mixture of SF₆ and C₄F₈.

To completely encapsulate the Si nanoposts, the first layer of PDMS (10:1 mixing ratio of Sylgard 184 base and curing agent) was diluted in toluene in a 2:3 weight ratio, which was spin-coated at 2500 rpm and cured at 80 °C for more than half an hour. The second layer of PDMS without dilution was subsequently spin-coated and cured at 80 °C for more than 2 h. The same procedure was used for both metasurface layers.

Measurement Method: A customized alignment system is shown in Figure 2b. The bottom metasurface layer was mounted on a rotation stage held by a vacuum pump, and the top layer was attached to a glass slide suspended by an XYZ translation stage. A drop of uncured PDMS was applied in between as an index-matched layer. The samples were then illuminated from the bottom by a collimated supercontinuum laser that was passed through a monochromator set at the designed working wavelength. The far-field images after the meta-optic were recorded by a near infrared (NIR) camera through an imaging system consisting of a 20 \times objective and a tube lens. A similar measurement was performed to observe the output intensity of the meta-optic, but with the imaging plane adjusted to be just beyond the second metasurface instead of in the far-field. The alignment holograms were then aligned by tuning the XYZ translation and rotation stage. After spatial alignment was achieved, the XY translation was further adjusted until the desirable far-field images were formed.

The efficiency was calculated based on the images captured by the NIR camera with the background noise correction processed by subtraction of a blank image, which contained the dark current signals. The reference intensity was calculated from images of the substrates without any meta-optics. With the same integration time, the intensity distribution was revealed by the photon count from the camera. The efficiency of the beam-former and splitter devices was calculated as the intensity within an area encompassing each beam in the far-field divided by the intensity incident on the device. For the 3D hologram example, the efficiency was calculated as the intensity contained in the transmitted field divided by the intensity incident on the device.

Supporting Information

Supporting Information is available from the Wiley Online Library or from the author.

Acknowledgements

This research was supported in part through computational resources and services provided by Advanced Research Computing at the University of Michigan, Ann Arbor. A portion of this research was conducted at the Center for Nanophase Materials Sciences, which is a DOE Office of Science User Facility. Finally, B.O.R. and A.G. are grateful to Cody Scarborough for assistance in creating the graphics. B.O.R. acknowledges the financial support by the National Science Foundation Graduate Research Fellowship Program under grant DGE 1256260. B.O.R., H.Z., Y.Z., J.V., and A.G. acknowledge the financial support by the Office of Naval Research under grant no. N00014-18-1-2536.

Conflict of Interest

The authors declare no conflict of interest.

Author Contributions

B.O.R. and H.Z. contributed equally to this work. B.O.R.: developed device designs, conducted simulations, and wrote the manuscript. H.Z. and Y.Z.: completed device fabrication and experimental measurements. I.I.K.: performed material growth. J.V. and A.G.: conceived the research concepts

and supervised the project. All authors discussed research results and participated in preparing the manuscript.

Data Availability Statement

The data that support the findings of this study are available from the corresponding author upon reasonable request.

Keywords

amplitude control, dielectric metasurfaces, holography, meta-optics

Received: October 20, 2021

Published online: December 26, 2021

-
- [1] N. Yu, F. Capasso, *Nat. Mater.* **2014**, *13*, 139.
- [2] I. Staude, J. Schilling, *Nat. Photonics* **2017**, *11*, 274.
- [3] Q. He, S. Sun, S. Xiao, L. Zhou, *Adv. Opt. Mater.* **2018**, *6*, 1800415.
- [4] S. M. Kamali, E. Arbabi, A. Arbabi, A. Faraon, *Nanophotonics* **2018**, *7*, 1041.
- [5] M. Khorasaninejad, W. T. Chen, R. C. Devlin, J. Oh, A. Y. Zhu, F. Capasso, *Science* **2016**, *352*, 1190.
- [6] Y. Zhou, I. I. Kravchenko, H. Wang, J. R. Nolen, G. Gu, J. Valentine, *Nano Lett.* **2018**, *18*, 7529.
- [7] D. Zhang, M. Ren, W. Wu, N. Gao, X. Yu, W. Cai, X. Zhang, J. Xu, *Opt. Lett.* **2018**, *43*, 267.
- [8] X. Zhang, R. Deng, F. Yang, C. Jiang, S. Xu, M. Li, *ACS Photonics* **2018**, *5*, 2997.
- [9] J. Li, C. Liu, T. Wu, Y. Liu, Y. Wang, Z. Yu, H. Ye, L. Yu, *Nanoscale Res. Lett.* **2019**, *14*, 34.
- [10] Y. Lin, M. Wang, Z. Sui, Z. Zeng, C. Jiang, *Jpn. J. Appl. Phys.* **2019**, *58*, 060918.
- [11] L. Liu, X. Zhang, M. Kenney, X. Su, N. Xu, C. Ouyang, Y. Shi, J. Han, W. Zhang, S. Zhang, *Adv. Mater.* **2014**, *26*, 5031.
- [12] X. Song, L. Huang, C. Tang, J. Li, X. Li, J. Liu, Y. Wang, T. Zentgraf, *Adv. Opt. Mater.* **2018**, *6*, 1701181.
- [13] L. Huang, S. Zhang, T. Zentgraf, *Nanophotonics* **2018**, *7*, 1169.
- [14] L. Huang, X. Chen, H. Mühlenbernd, H. Zhang, S. Chen, B. Bai, Q. Tan, G. Jin, K. W. Cheah, C. W. Qiu, J. Li, T. Zentgraf, S. Zhang, *Nat. Commun.* **2013**, *4*, 2808.
- [15] G. Y. Lee, G. Yoon, S. Y. Lee, H. Yun, J. Cho, K. Lee, H. Kim, J. Rho, B. Lee, *Nanoscale* **2018**, *10*, 4237.
- [16] A. C. Overvig, S. Shrestha, S. C. Malek, M. Lu, A. Stein, C. Zheng, N. Yu, *Light: Sci. Appl.* **2019**, *8*, 2047.
- [17] Q. Wang, X. Zhang, Y. Xu, J. Gu, Y. Li, Z. Tian, R. Singh, S. Zhang, J. Han, W. Zhang, *Sci. Rep.* **2016**, *6*, 32867.
- [18] H.-X. Xu, G. Hu, L. Han, M. Jiang, Y. Huang, Y. Li, X. Yang, X. Ling, L. Chen, J. Zhao, C.-W. Qiu, *Adv. Opt. Mater.* **2019**, *7*, 1801479.
- [19] H.-X. Xu, G. Hu, Y. Li, L. Han, J. Zhao, Y. Sun, F. Yuan, G.-M. Wang, Z. H. Jiang, X. Ling, T. J. Cui, C.-W. Qiu, *Light: Sci. Appl.* **2019**, *8*, 1.
- [20] H.-X. Xu, G. Hu, M. Jiang, S. Tang, Y. Wang, C. Wang, Y. Huang, X. Ling, H. Liu, J. Zhou, *Adv. Mater. Technol.* **2020**, *5*, 1900710.
- [21] G. Y. Lee, J. Y. Hong, S. H. Hwang, S. Moon, H. Kang, S. Jeon, H. Kim, J. H. Jeong, B. Lee, *Nat. Commun.* **2018**, *9*, 4562.
- [22] W.-J. Joo, J. Kyoung, M. Esfandyarpour, S.-H. Lee, H. Koo, S. Song, Y.-N. Kwon, S. H. Song, J. C. Bae, A. Jo, M.-J. Kwon, S. H. Han, S.-H. Kim, S. Hwang, M. L. Brongersma, *Science* **2020**, *370*, 459.
- [23] Y. Zhou, H. Zheng, I. I. Kravchenko, J. Valentine, *Nat. Photonics* **2020**, *14*, 316.
- [24] M. Faraji-Dana, E. Arbabi, A. Arbabi, S. M. Kamali, H. Kwon, A. Faraon, *Nat. Commun.* **2018**, *9*, 4196.
- [25] Y. Zhou, I. I. Kravchenko, H. Wang, H. Zheng, G. Gu, J. Valentine, *Light: Sci. Appl.* **2019**, *8*, 2047.
- [26] D. H. Kwon, G. Ptitsyn, A. Díaz-Rubio, S. A. Tretyakov, *Phys. Rev. Appl.* **2018**, *9*, 034005.
- [27] A. Epstein, G. V. Eleftheriades, *Phys. Rev. Lett.* **2016**, *117*, 256103.
- [28] D. H. Kwon, S. A. Tretyakov, *Phys. Rev. B* **2018**, *97*, 035439.
- [29] V. G. Ataloglou, G. V. Eleftheriades, in *2020 IEEE Int. Symp. on Antennas and Propagation and North American Radio Science Meeting*, IEEE, Piscataway, NJ **2020**, pp. 905–906.
- [30] J. Budhu, A. Grbic, *IEEE Trans. Antennas Propag.* **2021**, *69*, 122.
- [31] J. Li, A. Song, S. A. Cummer, *Phys. Rev. Appl.* **2020**, *14*, 044012.
- [32] B. O. Raeker, A. Grbic, *Phys. Rev. Lett.* **2019**, *122*, 113901.
- [33] B. O. Raeker, A. Grbic, *Phys. Rev. Appl.* **2021**, *15*, 054039.
- [34] A. S. Backer, *Opt. Express* **2019**, *27*, 30308.
- [35] V. G. Ataloglou, A. H. Dorrah, G. V. Eleftheriades, *IEEE Trans. Antennas Propag.* **2020**, *68*, 7382.
- [36] T. Brown, P. Mojabi, *TechRxiv (preprint at)* **2020**.
- [37] A. Arbabi, E. Arbabi, S. M. Kamali, Y. Horie, S. Han, A. Faraon, *Nat. Commun.* **2016**, *7*, 13682.
- [38] A. Arbabi, E. Arbabi, Y. Horie, S. M. Kamali, A. Faraon, *Nat. Photonics* **2017**, *11*, 415.
- [39] X. Huang, S. Shrestha, A. Overvig, N. Yu, in *2020 Conf. on Lasers and Electro-Optics (CLEO)*, San Jose, CA **2020**, pp. 1–2.
- [40] P. Georgi, Q. Wei, B. Sain, C. Schlickriede, Y. Wang, L. Huang, T. Zentgraf, *Sci. Adv.* **2021**, *7*, 9718.
- [41] X. Lin, Y. Rivenson, N. T. Yardimci, M. Veli, Y. Luo, M. Jarrahi, A. Ozcan, *Science* **2018**, *361*, 1004.
- [42] C. Qian, X. Lin, X. Lin, J. Xu, Y. Sun, E. Li, B. Zhang, H. Chen, *Light: Sci. Appl.* **2020**, *9*, 2047.
- [43] R. Gerchberg, W. Saxton, *Optik* **1972**, *35* 237.
- [44] A. Arbabi, Y. Horie, M. Bagheri, A. Faraon, *Nat. Nanotechnol.* **2015**, *10*, 937.
- [45] J. P. Balthasar Mueller, N. A. Rubin, R. C. Devlin, B. Groever, F. Capasso, *Phys. Rev. Lett.* **2017**, *118*, 113901.
- [46] C. Pfeiffer, A. Grbic, *Appl. Phys. Lett.* **2013**, *102*, 231116.
- [47] R. Pestourie, C. Pérez-Arancibia, Z. Lin, W. Shin, F. Capasso, S. G. Johnson, *Opt. Express* **2018**, *26*, 33732.
- [48] A. F. Oskooi, D. Roundy, M. Ibanescu, P. Bermel, J. D. Joannopoulos, S. G. Johnson, *Comput. Phys. Commun.* **2010**, *181*, 687.
- [49] J.-H. Park, *J. Inf. Disp.* **2017**, *18*, 1.
- [50] K. Matsushima, S. Nakahara, *Appl. Opt.* **2009**, *48*, H54.
- [51] K. Matsushima, *Appl. Opt.* **2005**, *44*, 4607.
- [52] K. Matsushima, H. Nishi, S. Nakahara, *J. Electron. Imaging* **2012**, *21*, 023002.
- [53] T. Phan, D. Sell, E. W. Wang, S. Doshay, K. Edee, J. Yang, J. A. Fan, *Light: Sci. Appl.* **2019**, *8*, 48.
- [54] M. Mansouree, H. Kwon, E. Arbabi, A. McClung, A. Faraon, A. Arbabi, *Optica* **2020**, *7*, 77.
- [55] R. C. Devlin, M. Khorasaninejad, W. T. Chen, J. Oh, F. Capasso, *Proc. Natl. Acad. Sci.* **2016**, *113*, 10473.
- [56] P. Kovesi, arXiv **2015**.